Check for updates

This article can be cited before page numbers have been issued, to do this please use: Y. Li, H. Li, Q. Guan, H. Ye, C. Zhang, L. Xu, H. Zhong, X. Zhou and J. Luo, *Inorg. Chem. Front.*, 2026, DOI: 10.1039/D5QI02302E.

View Article Online
DOI: 10.1039/D5QI02302E

Dual-site Hydrogen Bonding in 3D Hybrid Halide Perovskitoid Towards Stable and Sensitive Ultraviolet Light Detection

Yao Li, [a] Hang Li, [a] Qianwen Guan, [a] Huang Ye, [a] Chengshu Zhang, [a,c] Lijun Xu, [a] Haiqing Zhong, [a,b] Xinwei Zhou, [a] Junhua Luo* [a,d]

Three-dimensional (3D) organic-inorganic hybrid perovskites (OIHPs) are known for excellent charge transport and large light absorption coefficients, making them promising materials for ultraviolet (UV) photodetection. However, the traditional 3D ABX_3 perovskite structure is constrained by the tolerance factor, limiting its capacity to accommodate larger A-site cations. Therefore, it is necessary to explore novel 3D perovskitoids that can incorporate larger organic cations for UV photodetection. Herein, we introduced the diamine 3-methylaminopropylamine (3-MAPA) cation into the lead-iodide framework and successfully synthesized a 3D perovskitoid compound $(3\text{-MAPA})Pb_2I_6$ (MPI). By forming extensive network of hydrogen bonds between the 3-MAPA^{2+} cations and the inorganic framework, MPI effectively suppresses ion migration, thereby achieving ultralow dark-current drift of 8.184×10^{-8} nA cm^{-1} s^{-1} V^{-1}. Owing to its 3D inorganic lattice, MPI exhibits high carrier mobility-lifetime product ($\mu\tau$) of 2.613×10^{-3} cm^2 V^{-1}. These synergistic effects of extensive hydrogen bonding and 3D lead-halide framework collectively enable stable UV photodetection under periodic 377 nm illumination with high responsivity ($R \approx 464.42$ mA W^{-1}) and detectivity ($D^* \approx 4.05 \times 10^{12}$ Jones). This work establishes stable UV photodetection via 3D perovskitoid compound, expanding the candidate materials.

Introduction

Ultraviolet (UV) photodetection technology plays indispensable role in national defense, [1] environmental monitoring, [2] and biomedical applications.[3] However, mainstream UV photodetector materials (e.g., GaN, [4] AlGaN,[5] diamond, [6] AlN[7]) are hindered by high-temperature fabrication processes and escalating production costs. [8,9] These shortcomings severely limit their practical deployment in UV photodetection. [10-14] In recent years, organic-inorganic hybrid perovskites (OIHPs) are considered highly promising for UV photodetection due to their tunable bandgaps, strong light absorption, high charge-carrier mobility, and low-cost solution processability. [15-19] Among them, 3D perovskites exhibit exceptional performance in UV detection, featuring high sensitivity, ultrafast response, and low detection limits, [20-22] which are attributed to their 3D charge transport networks, superior light absorption efficiency and low exciton binding energy. [23] However, conventional 3D perovskites usually suffer from inherent phase instability, undergoing rapid decomposition under moisture, heat, and UV irradiation, which significantly compromises device operational lifetime.[24-27] Therefore, it is crucial to develop ultraviolet photodetectors that exhibit excellent stability and outstanding semiconductor properties.

Enhancement of the environmental stability of OIHPs materials is commonly achieved through modifications at the molecular level, including compositional engineering [28] and

dimensional control [29]. For instance, researchers have synthesized a series of two-dimensional hybrid perovskites by incorporating chain-like or aromatic amines into the metal-halide framework (e.g. $(BA)_2PbBr_4$, [30] $(i\text{-}BA)_2(MA)Pb_2Cl_7$,[31] $(C_8H_{11}FN)_2PbBr_4$,[32] et al.), which effectively suppresses ion migration and enhances ultraviolet photochemical stability. However, restricted by the Goldschmidt tolerance factor, [33-37] the introduction of bulky cations leads to the separation of inorganic and organic layers. These low-dimensional perovskites exhibit significant quantum confinement effects, which impede carrier transport and consequently hinder the development of high-performance UV photodetectors. [38-42] In recent years, 3D hybrid perovskitoids materials with extended lattices have attracted widespread attention due to their capability to accommodate larger organic cations, [43] offering a promising avenue for designing stable 3D structure. These structures feature both corner-sharing and edge-sharing octahedral connectivity, enabling the accommodation of larger A-site cations by breaking the traditional constraints of the tolerance factor. Inspired by this concept, researchers have synthesized novel 3D perovskitoids (e.g. $(3\text{-MAPA})Pb_2Br_6$[44] and $(DMPZ)Pb_2Br_6$, [45] et al.) and integrated them into X-ray detectors, yielding devices that are exceptionally stable and high carrier mobility. The performance enhancement originates from form extensive network of hydrogen bonds between the diamine cations and the inorganic framework, which effectively suppresses ion migration, while the preserved 3D inorganic scaffold facilitates efficient charge carrier transport. [46,47] Extending this strategy to UV photodetection, the exploration of diamine-derived 3D perovskitoids compounds holds significant promise.

Here, by incorporating the diammonium cation 3-methylaminopropylammonium (3-MAPA) into metal-halide framework, we have successfully synthesized a novel 3D perovskitoid $(3\text{-MAPA})Pb_2I_6$ (MPI)—featuring conformationally diverse organic cations. Abundant hydrogen bonds interaction

a. State Key Laboratory of Functional Crystals and Devices, Fujian Institute of Research on the Structure of Matter, Chinese Academy of Sciences, Fuzhou, Fujian 350002, China.
E-mail: jhluo@fjirsm.ac.cn
b. College of Chemistry, Fuzhou University, Fuzhou, Fujian 350108, China
c. School of Physical Science and Technology, ShanghaiTech University, Shanghai 201210, China
d. Fujian College, University of Chinese Academy of Sciences, Fuzhou 350000, China

between the diamine cations and the inorganic lattice overcome the conventional tolerance-factor limitations associated with 3D perovskites. The 3D inorganic framework endows MPI with high carrier mobility-lifetime product ($\mu\tau$ = 2.613×10^{-3} cm^2 V^{-1}). Devices fabricated from MPI single crystals demonstrate high responsivity (R ≈ 464.42 mA W^{-1}) and specific detectivity (D* ≈ 4.05×10^{12} Jones), and exhibit excellent operational light stability under periodic 377 nm illumination. Additionally, under 10 V bias and sustained ON/OFF switching over 10^3 cycles, the photocurrent remains stable without degradation. Crucially, the dark current drift at 10 V over 1000 seconds is extremely low, at 8.184×10^{-8} nA cm^{-1} s^{-1} V^{-1}. MPI also demonstrates significantly superior environmental stability relative to conventional 3D hybrid perovskites. This work provides a new perspective on the application of perovskitoids in UV photodetection by elucidating the critical role of hydrogen bonding in enhancing material performance and stability.

Results and Discussion

Micromorphology and Optoelectronic Properties

Large red single crystals of (3-MAPA)Pb$_2$I$_6$ (MPI) with dimensions of 8 × 2 × 16 mm^3 were successfully synthesized via slow-cooling solution method (**Figures S1 and S2**). Scanning electron microscopy (SEM) and atomic force microscopy (AFM) analyses revealed smooth and well-faceted morphology (Figures S3 and S4), indicating low density of surface defects. Such high crystal quality is beneficial for minimizing surface trap states and enhancing the transport of photogenerated charge carriers. Phase purity was confirmed by powder X-ray diffraction (PXRD), where the experimental pattern exhibited sharp and intense reflections in excellent agreement with the simulated pattern (Figure S5), indicating high-purity, single-phase material with excellent quality. High-resolution rocking curve measurements of the (080) plane yielded narrow full width at half maximum (FWHM) of 0.018° (Figure S6), indicative of minimal mosaicity and exceptional lattice coherence throughout the crystal. This exceptional material quality facilitates comprehensive investigation of the intrinsic stability and ultraviolet photoresponse under low-intensity illumination.

Single-crystal X-ray diffraction analysis revealed that MPI crystallizes in the orthorhombic *Pbam* space group (Table S1). The structure comprises 3D framework constructed from edge-sharing [Pb$_2$I$_{10}$]$^{6-}$ dimers, which are further interconnected via corner-sharing to form an extended network along the [001] direction (**Figures 1a-c and S7**). The coexistence of edge-sharing and corner-sharing motifs along different crystallographic axes induces pronounced structural anisotropy, leading to direction-dependent charge transport and photoresponse behaviors. This unique topology creates well-defined cavities capable of accommodating the bulky divalent organic cation 3-MAPA^{2+}. MPI crystal accommodates two distinct molecular conformations within its framework cavities. While the N-H···I

hydrogen bonds are a hallmark of conventional 3D perovskite, the emergence of C-H···I interactions is particularly noteworthy: the conformation of the 3-MAPA^{2+} cation brings C-H moieties into closer proximity to I sites (Figure S8). Additionally, the local electrostatic influence of the NH$_3^+$ group enhances delocalization of hydrogen electron density, thereby activating the C-H group as hydrogen-bond donor and enabling formation of the C-H···I hydrogen bond.[48] To better understand the interactions within the molecule, we performed Hirschfeld surface analysis using Crystal Explorer software, where the red regions indicate stronger hydrogen bond intermolecular forces between N-H···I and C-H···I (Figure 1d). Compared with single-amine cations, in the A'Pb2I6 perovskite built from diammonium cations we observe relatively rich hydrogen-bond network between the organic cations and the inorganic framework (Figure1e, Table S2).[49] Such an extensive hydrogen-bonding network is contribute to enhanced structural stability. Moreover, the existence of multiple conformations of the organic cation enables multidirectional hydrogen-bond formation with the inorganic lattice, enhancing crystallographic symmetry and suppressing lattice distortion. This is evidenced by the notably lower calculated (Distortion index D = 0.00516, the bond angles variance σ^2 = 1.92167) of MPI relative to other diammonium A'Pb$_2$I$_6$ perovskites (Figures 1f and S8, Tables S3-S4). Different conformational states of organic cations can reinforce crystal rigidity and moisture resistance by modulating hydrogen-bonding networks and electrostatic interactions, thereby improving phase stability.[50,51]

In general, the application of 3D perovskites in optoelectronic devices is primarily governed by their intrinsic semiconductor and optical properties. Therefore, we employed synergistic approach combining first-principles calculations with experimental characterization. The UV-vis absorption spectrum exhibits a sharp absorption edge around 606 nm, corresponding to optical bandgap (E_g) of 2.13 eV, as determined by Tauc plot analysis (**Figure 2a**). Density functional theory (DFT) calculations reveal that MPI possesses direct bandgap with both the valence band maximum (VBM) and conduction band minimum (CBM) located at the same Brillouin zone. The calculated bandgap of 2.12 eV (Figure 2b) aligns well with the experimental value, indicating the reliability of the employed computational approach. Under 450 nm excitation, MPI exhibits a pronounced photoluminescence (PL) peak at 584 nm (Figure S9), corresponding to an optical bandgap of approximately 2.12 eV, as determined using the photon energy equation. The intense PL emission indicates efficient radiative recombination, highlighting MPI's potential for optoelectronic applications. Partical density of states (PDOS) analysis indicates that the VBM is primarily composed of iodine 5p orbitals, while the CBM is dominated by lead 6p orbitals, confirming that the electronic transitions are largely governed by the inorganic sublattice (Figure 2c). Partial charge density mappings (Figure S10) further illustrate that electronic states near the VBM are predominantly localized around equatorial I atoms, whereas CBM states are
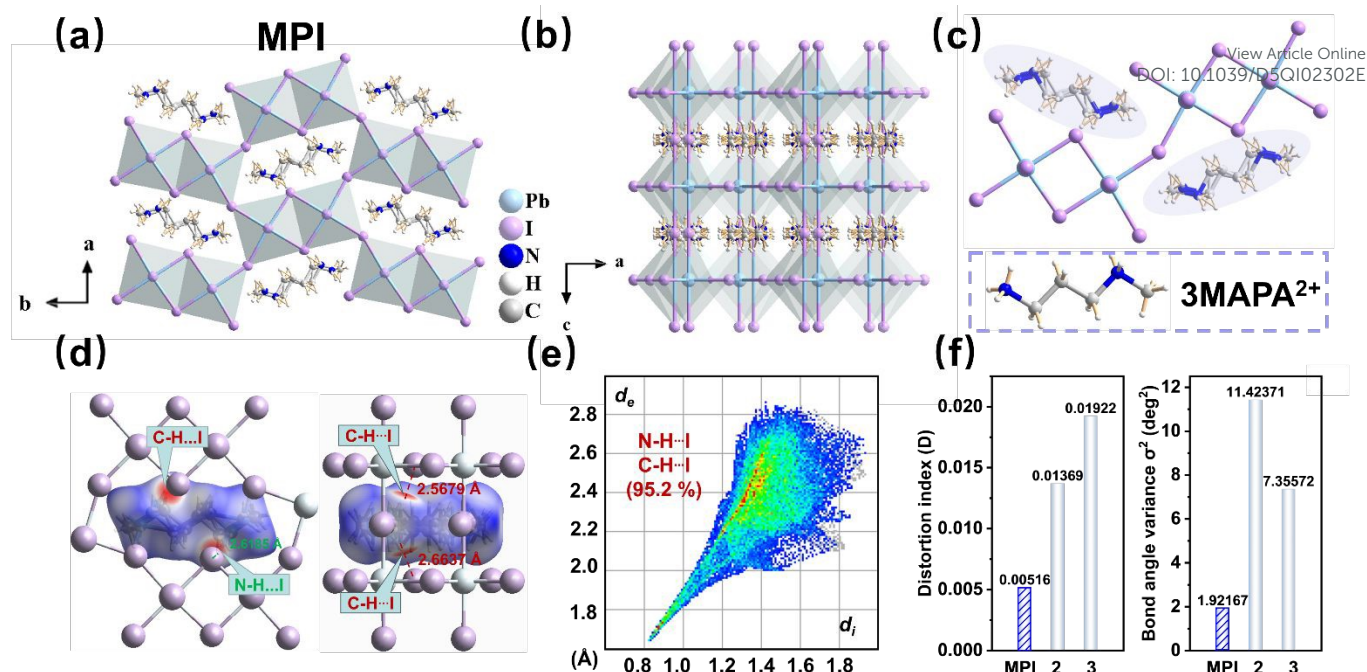
Figure 1. (a) Crystal structure of MPI viewed along the *c*-axis. (b) Crystal structure of MPI viewed along the *b*-axis. (c) Two distinct molecular conformations of 3-MAPA^{2+} within the structural voids (inset: molecular structure of 3-MAPA). (d) Hirshfeld d_{norm} surface of 3-MAPA^{2+}. (e) Two-dimensional fingerprint plot of 3-MAPA^{2+}. (f) Comparative analysis of distortion and bond angle variance in MPI and other 3D diammonium lead iodide perovskitoids.

concentrated around Pb centers, indicative of strong electronic anisotropy. This electronic anisotropy is structurally rooted in the unique coexistence of edge-sharing and corner-sharing [PbI$_6$] octahedra along distinct crystallographic axes (Figure 1a), which induces pronounced structural anisotropy. The Pb-I-Pb bond angles along the *a* and *b* axes (151.43° and 92.20°, respectively) deviate more from linearity than the *c*-axis (179.36°) (Figure S11), leading to differences in charge distribution and optical transition probabilities.

The crystallographic anisotropy manifests as distinct direction-dependent charge transport characteristics. To further elucidate the optoelectronic properties of MPI, we fabricated devices along different crystallographic axes and systematically characterized their carrier mobility (Figure S12) and photoresponse (Figure S13). The mobility-lifetime product ($\mu\tau$), a critical parameter reflecting charge transport efficiency in ultraviolet photodetectors, was quantitatively extracted using a modified Hecht equation, which describes the average carrier drift distance under an applied electric field. [52,53]

$$I = \frac{I_0 \mu\tau V}{L^2}\left[1 - \exp\left(-\frac{L^2}{\mu\tau V}\right)\right]$$

where I is the photocurrent, I_0 is the saturation photocurrent, V is the applied bias voltage, L is the inter-electrode distance, μ is the carrier migration, and τ is the carrier lifetime. Remarkably, MPI exhibits exceptional charge transport properties, with the *c*-axis-oriented device demonstrating the highest $\mu\tau$ product of 2.613×10^{-3} cm^2 V^{-1} (Figure 2d), significantly surpassing values

obtained along the *a*-axis (1.705×10^{-3} cm^2 V^{-1}) and *b*-axis (1.076×10^{-3} cm^2 V^{-1}) (Figure S12). This indicates superior charge transport efficiency along the *c*-axis, significantly surpassing that of most reported perovskite materials, which is particularly beneficial for overall photodetector performance (Table S5). For directional photoresponse evaluation under 377 nm UV illumination, comparative analysis of dark current and photocurrent in *a*, *b*, and *c*-axis devices revealed that the *c*-axis device achieves the maximum switching ratio of 1586, substantially exceeding values from other orientations (Figure S13). This superior *c*-axis performance results from the interplay between high carrier mobility and improved photoinduced charge separation in this direction. Based on these findings, we conducted comprehensive photodetection analysis specifically on the optimal *c*-axis-oriented devices.

To comprehensively evaluate the semiconductor properties of the material, we systematically investigated the charge transport characteristics and photoresponse behavior of photoconductive devices based on MPI. The defect density of MPI was evaluated using the space-charge-limited current (SCLC) method. [54] Figure 2e reveals three characteristic regimes: (1) an ohmic region ($n = 1$) at low bias, (2) a trap-filled limit (TFL) region ($n = 2$) at intermediate bias, and (3) the child's region ($n > 3$). This behavior suggests trap-dominated charge injection. The trap density (n_{trap}) was derived from the following equation:

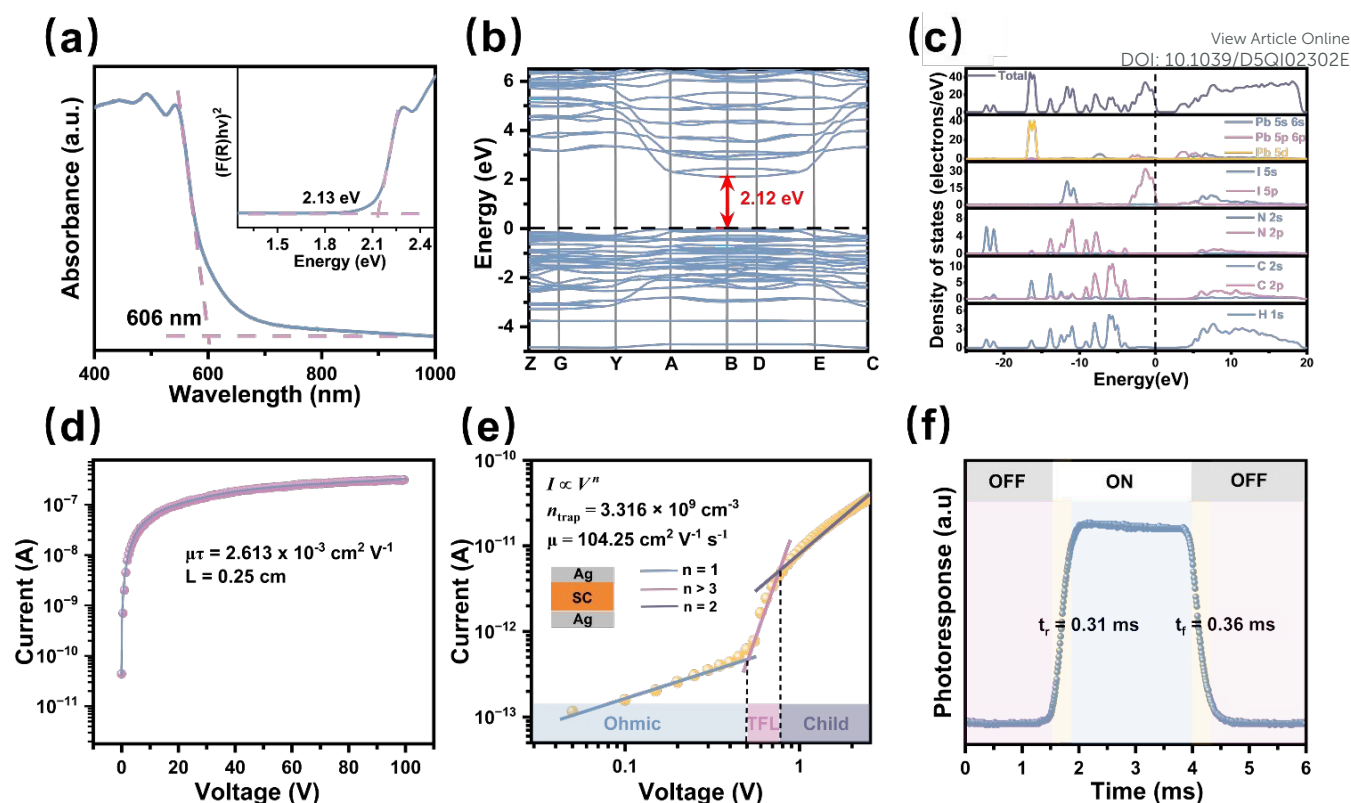$$n_{trap} = \frac{2\varepsilon\,\varepsilon_0 V_T}{qL^2}$$

Figure 2 . (a) Absorption spectra of MPI. The inset shows the diffuse-reflectance spectrum. The calculated electronic band structure (b) and DOS (c) of MPI. (d) The carrier mobility-lifetime ($\mu\tau$) product of MPI. (e) Logarithmic I-V curves were measured by using the SCLC method. (f) The rise and fall response times of an optical switch.

where V_T is the threshold voltage, L is the thickness, q denotes the electron charge, ε and ε_0 denote the relative and vacuum dielectric constant, respectively. The extracted trap density is 3.316×10^9 cm^{-3}, indicating low defect density and reduced nonradiative recombination, which contributes to enhanced device photoresponsivity. The hole-only carrier mobility (μ) determined from the Child region using the Mott-Gurney power law:

$$\mu = \frac{8JL^3}{9\varepsilon\varepsilon_0 V^2}$$

the μ value of (3-MAPA)Pb$_2$I$_6$ along the c-axis direction was calculated to be 104.25 cm^2 V^{-1} s^{-1}. Furthermore, based on the slope of the I-V curve, the resistivity (ρ) of MPI was determined to be 1.14×10^{10} Ω cm, indicating high intrinsic resistivity (Figure S14). This suggests low carrier concentration under dark conditions, which is advantageous for improving detection sensitivity. Notably, this resistivity is significantly higher than that of conventional 3D perovskites such as MAPbBr$_3$, CsPbBr$_3$, and MAPbI$_3$ (typically in the range of 10^6-10^9 Ω cm),[55-57] enabling effective suppression of dark current and noise, thereby promoting more stable and sensitive photodetection. The temporal response of the photodetector, defined by the rise (τ_{rise}) and fall (τ_{fall}) times corresponding to increase from 10% to 90% and decay from 90% to 10% of photocurrent, is a key indicator of device performance. MPI demonstrates rapid switching behavior, with τ_{rise} = 206 μs and τ_{fall} = 230 μs,

underscoring its suitability for high-speed optoelectronic applications (Figure 2f).

Performance of UV Detection

Superior semiconductor properties are fundamental to achieving high-performance photodetectors. To evaluate the semiconductor characteristics and photodetection potential of MPI, planar electrode photodetector was fabricated along the c-axis, which favors efficient carrier transport, based on high-quality MPI single crystals (**Figure 3a**). Photocurrent measurements across the 266 - 637 nm wavelength range revealed photoresponse consistent with the absorption spectrum, with a peak observed at 377 nm under an illumination intensity of 4.965 mW cm^{-2} (Figure 3b). Consequently, the irradiation of 377 nm laser was selected for further photoelectrical performance. Under 377 nm ultraviolet illumination, the device exhibited pronounced photoresponse, as the photocurrent density increased with increasing light intensity (Figure 3c). Notably, the device demonstrated ultralow dark current of only 9.9×10^{-11} A, and under illumination intensity of 4.965 mW cm^{-2} with 10 V bias, it generated photocurrent of 1.57×10^{-7} A, yielding high on/off current ratio of 1586, indicative of its excellent light responsiveness. The photocurrent remained stable and discernible through repeated light on/off switching cycles, demonstrating both sensitivity and operational stability under low light power (Figure 3d). This capability is attributed to the low defect density and superior charge transport in the MPI single crystal, which
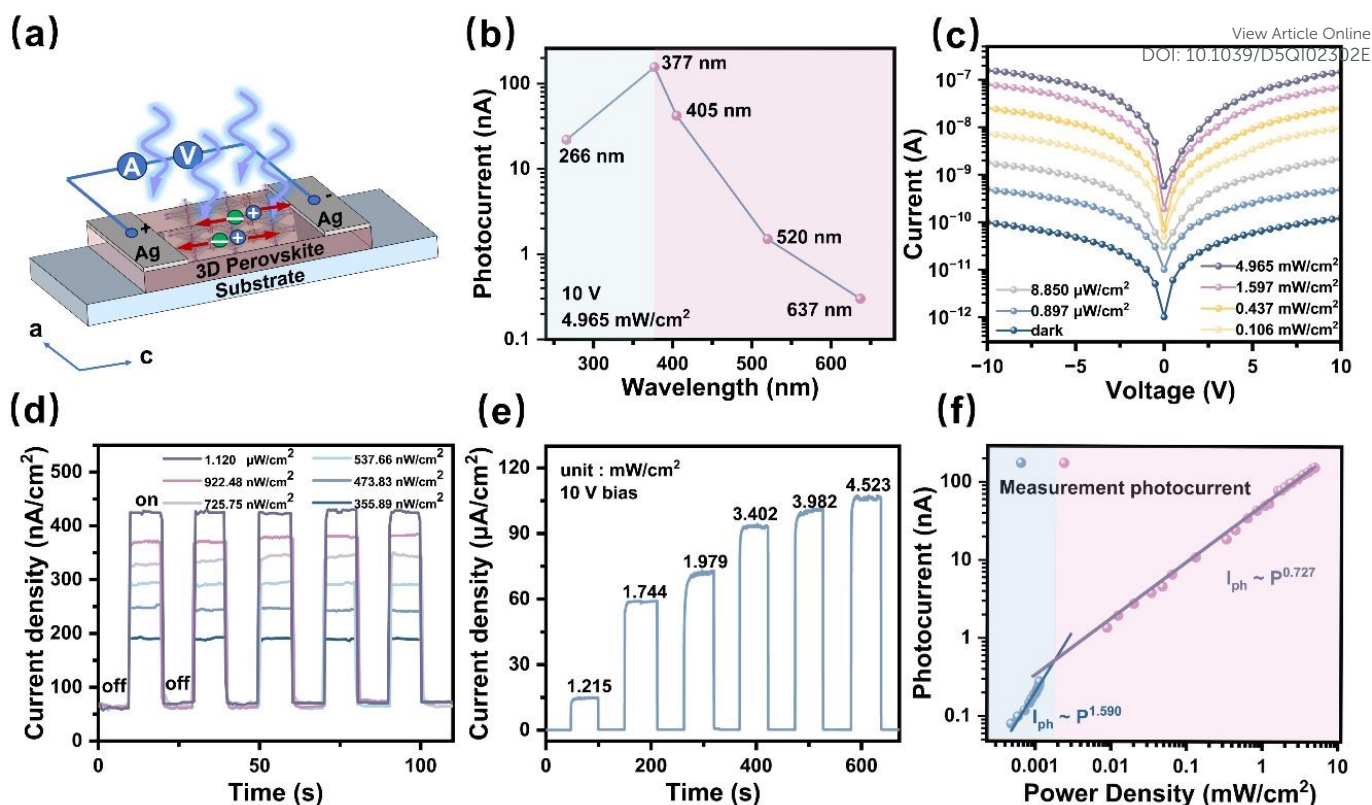
Figure 3. Photoelectric properties of MPI. (a) Schematic illustration of the MPI based photodetector under 377 nm UV illumination. (b) The photoelectric response at different wavelength light with the illumination of 4.965 mW cm^{-2} and 10 V bias. (c) I-V characteristics of the device at different optical power densities. (d) I-t diagram of weak light at 377 nm UV illumination. (e) Photoresponse of the detector to optical power ranging from 1.215 to 4.523 mw cm^{-2} at 10 V bias under fresh air conditions. (f) Dependence of photocurrent (I_{ph}) on optical power density at 377 nm.

enabled low detection limit down to the nW cm^{-2} level, showing significant potential for UV signal detection. Furthermore, under 10 V bias voltage, the device showed linear increase in photocurrent with increasing light intensity from 1.215 to 4.523 mWcm^{-2} (Figure 3e), further confirming its excellent linear response. To elucidate the detector's enhanced performance under low light, the relationship between photocurrent ($I_{ph} = I_{light} - I_{dark}$) and incident light power density (P) was analyzed using the empirical power law $I_{ph} \sim P^{\beta}$ (Figure 3f). This model describes the photoresponse behavior across different illumination intensities, where the exponent β reflects the sensitivity of the device to light intensity and is closely linked to the photogeneration, trapping, and recombination of carriers. Fitting results revealed that under light, the β value reached 1.590, which is markedly higher than 0.727 under strong illumination. This elevated β indicates more efficient photoresponse at low intensities, likely due to suppressed carrier recombination and enhanced charge extraction, thereby improving detection sensitivity. In conclusion, the MPI-based UV photodetector exhibits excellent photoresponse characteristics under illumination, suggesting great potential for applications in low-intensity ultraviolet detection, such as environmental monitoring, biosensing, and early warning systems.

The MPI based photodetector exhibits pronounced and stable photoresponse along the *c*-axis under ultraviolet (UV) illumination, characterized by high responsivity (R) and specific detectivity (D*) values. Both R and D* decrease with increasing incident light power density, following power-law decay, which is typically associated with carrier recombination mechanisms (**Figure 4a**). At low power densities, the device achieves responsivity of 464.42 mA W^{-1} and detectivity of 4.051 × 10^{12} Jones, indicating its superior sensitivity to UV light. Notably, the MPI based photodetector demonstrates exceptional R and D*, surpassing most perovskite materials employed in photoelectric detection, including (BPA)$_2$PbBr$_4$[53], (PA)$_2$PbBr$_4$, [49] (*i*-PA)$_2$CsAgBiBr$_7$, [58] and MAPbI$_3$ nanoribbon arrays [59] (Figure 4b, Table S6). The MPI photodetector demonstrates exceptional photostability under periodic ultraviolet (UV) illumination at 377 nm, with the photocurrent maintaining 98.5% of its initial value after 1000 s of multiple cycle testing (Figure 4c). Further investigation into the photoresponse dynamics reveals pronounced and rapid on/off switching behavior under periodic UV excitation, indicating swift response times suitable for high-frequency communication and fast imaging applications. After 10^3 consecutive light on/off cycles under 10 V bias, the photocurrent remains stable without significant degradation, highlighting the device's reliability and fatigue resistance (Figure 4d). Environmental stability assessments show remarkable resistance to degradation, with the device retaining 96.5% of its
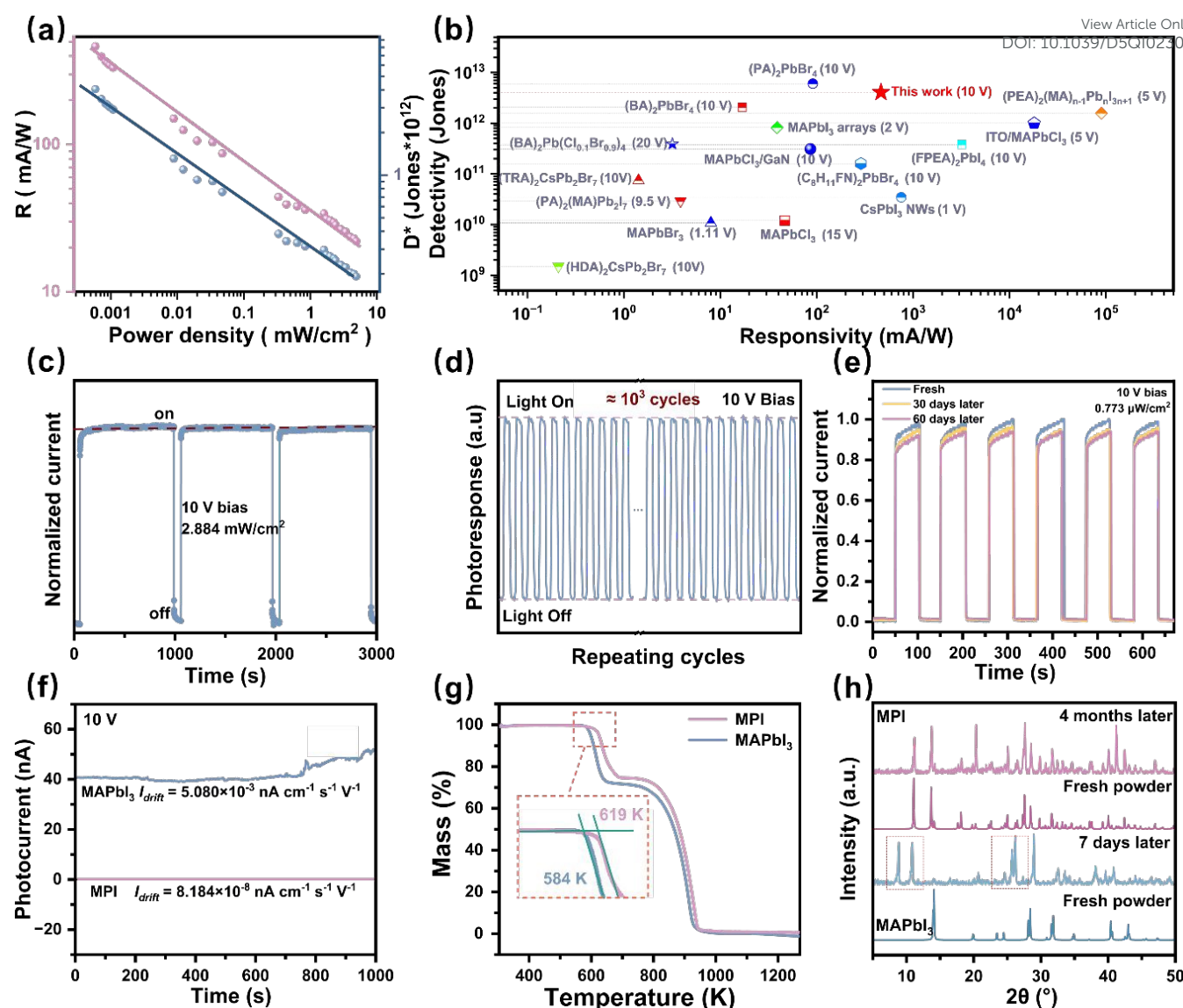
Figure 4. (a) Responsivity (R) and detectivity (D*) of MPI as function of incident light power density. (b) Comparison of R and D* for previously reported materials. (c) Radiation stability of the detector under continuous 377 nm wavelength illumination. (d) Repetitive switching cycles ≈ 10^3 of photoresponse under 10V bias. (e) Photoresponses of MPI detector to UV light at 10 V in fresh, 30 days later and 60 days later. (f) Dark current tracking of MPI and $MAPbI_3$ detector at 10 V. (g) TGA curve of the MPI and $MAPbI_3$ showing thermal stability. (h) PXRD patterns of MPI and $MAPbI_3$.

initial photoresponse after 60 days of storage under ambient conditions (25°C, 40-60% RH) (Figure 4e). To more intuitively evaluate the device performance and stability of the materials, comparative study was conducted between MPI and the conventional 3D perovskite $MAPbI_3$ in terms of dark current drift, thermal robustness, and structural stability. Dark current drift (I_{drift}) was employed as quantitative indicator of the dark-state stability of the photodetectors, calculated using the following equation:

$$I_{drift} = \frac{I_t - I_0}{E \times A \times t}$$

where I_t and I_0 represent the current at time, and the initial current, respectively, E and A denote the electric field and device area. Under an applied bias of 10 V, the MPI-based device exhibited an ultra-low I_{drift} value of 8.184 × 10^{-8} nA cm^{-1} s^{-1} V^{-1} (Figure 4f). Notably, MPI maintained excellent dark current stability under prolonged external electric fields, exhibiting significantly lower dark-current drift than most perovskite materials (Table S5). This enhanced stability is attributed to the presence of conformationally diverse cations in MPI, which form abundant non-covalent interactions that effectively suppress ion migration and stabilize the dark current. In terms of thermal stability, thermogravimetric analysis (TGA) revealed that the decomposition temperature of MPI reaches 612 K, significantly higher than that of $MAPbI_3$ (570 K), and surpassing many reported OIHPs (Figure 4g). Furthermore, X-ray diffraction (XRD) patterns confirmed that MPI retained its

crystalline structure after storage under 50% relative humidity for four months, with no detectable formation of secondary phases or notable peak attenuation (Figure 4h). In contrast, MAPbI$_3$ showed pronounced degradation within just one week under identical conditions. The exceptional structural and environmental stability of MPI is ascribed to the synergistic effect between the multi-conformational cationic arrangement and the diamine-anchored topological network structure. This work represents the first demonstration of utilizing multi-conformational 3D perovskitoid material to construct high-performance ultraviolet photodetectors with outstanding long-term stability, thereby advancing the development of reliable UV detection technologies.

Conclusions

In summary, we synthesized a novel 3D perovskitoid material designated as (3-MAPA)Pb$_2$I$_6$ (MPI) and systematically investigated its potential for ultraviolet light photodetection. By forming an extensive network of hydrogen bonds between the 3-MAPA^{2+} cations and the inorganic framework, MPI effectively suppresses ion migration, thereby achieving ultralow dark-current drift of 8.184×10^{-8} nA cm^{-1} s^{-1} V^{-1}. Benefiting from the structural advantages of its 3D inorganic framework, the MPI detector exhibits exceptional carrier mobility-lifetime product ($\mu\tau = 2.613 \times 10^{-3}$ cm^2 V^{-1}). These synergistic effects of extensive hydrogen bonding and 3D lead-halide framework collectively enable stable UV photodetection under periodic 377 nm illumination with high responsivity (R $\approx$ 464.42 mA W^{-1}) and detectivity (D* $\approx$ 4.05×10^{12} Jones). This work presents novel design strategy for 3D hybrid perovskitoid, based on their high responsivity, excellent stability, and ultralow detection limit down to the nW cm^{-2} level, which provides new pathway for constructing high-performance UV photodetectors.

Author contributions

Yao Li wrote the manuscript; Hang Li and Qianwen Guan performed the data analysis; Huang Ye and Chengshu Zhang performed the validation; Lijun Xu, Haiqing Zhong and Xinwei Zhou performed the data curation; Junhua Luo performed the methodology and reviewed this article.

Conflicts of interest

The authors declare no conflict of interest.

Data availability

The data that support the findings of this study are available in the supplementary material of this article. CCDC 2486626 contains the supplementary crystallographic data for this paper. These data can be obtained free of charge from The Cambridge Crystallographic Data Centre via www.ccdc.cam.ac.uk/data_request/cif.

References

1   Y. Zhang, Y. Cai, J. Zhou, Y. Xie, Q. Xu, Y. Zou, S. Guo, H. Xu, C. Sun and S. Liu, Surface acoustic wave-based ultraviolet photodetectors: a review, *Sci. Bull*, 2020, **65**, 587-600.
2   L. Jia, W. Zheng and F. Huang, Vacuum-ultraviolet photodetectors, *PhotoniX*, 2020, **1**, 1-25.
3   H. Chen, K. Liu, L. Hu, A. A. Al-Ghamdi and X. Fang, New concept ultraviolet photodetectors, *Mater. Today*, 2015, **18**, 493-502.
4   D. Y. Um, B. Chandran, J. Y. Kim, J. K. Oh, S. U. Kim, J. U. An, C. R. Lee and Y. H. Ra, New Charge Carrier Transport-Assisting Paths in Ultra-Long GaN Microwire UV Photodetector, *Adv. Funct. Mater.*, 2023, **33**, 2306143.
5   Q. Cai, H. You, H. Guo, J. Wang, B. Liu, Z. Xie, D. Chen, H. Lu, Y. Zheng and R. Zhang, Progress on AlGaN-based solar-blind ultraviolet photodetectors and focal plane arrays, *Light-Sci Appl*, 2021, **10**,1-31.
6   E. Pace, R. Di Benedetto and S. Scuderi, Fast stable visible-blind and highly sensitive CVD diamond UV photodetectors for laboratory and space applications, *Diam Relat Mater*, 2000, **9**, 987-993.
7   H. Wu, C. Wu, X. Cheng, C. Guo, J. Hu, D. Guo and S. He, Highly Wavelength-Selective Self-Powered Solar-Blind Ultraviolet Photodetector Based on Colloidal Aluminum Nitride Quantum Dots, *Small*, 2025, **21**, 2312127.
8   W. Guo, H. Xu, W. Weng, L. Tang, Y. Ma, Y. Liu, L. Hua, B. Wang, J. Luo and Z. Sun, Broadband Photoresponses from Ultraviolet to Near-Infrared (II) Region through Light-induced Pyroelectric Effects in a Hybrid Perovskite, *Angew. Chem. Int. Ed*, 2022, **61**, e202213477.
9   Z. Huo, Y. Zhang, X. Han, W. Wu, W. Yang, X. Wang, M. Zhou and C. Pan, Piezo-phototronic effect enhanced performance of a p-ZnO NW based UV-Vis-NIR photodetector, *Nano Energ*, 2021, **86**, 106090.
10 Z. Jin, Q. Zhou, Y. Chen, P. Mao, H. Li, H. Liu, J. Wang and Y. Li, Graphdiyne : ZnO Nanocomposites for High-Performance UV Photodetectors, *Adv. Mater*, 2016, **28**, 3697-3702.
11 Y. Ping, H. Long, H. Liu, C. Chen, N. Zhang, H. Jing, J. Lu, Y. Zhao, Z. Yang, W. Li, F. Ma, X. Fang, Z. Wei and H. Xu, Polarization Sensitive Solar-Blind Ultraviolet Photodetectors Based on Ultrawide Bandgap KNb$_3$O$_8$ Nanobelt with Fringe-Like Atomic Lattice, *Adv. Funct. Mater.*, 2022, **32**, 2111673.
12 H. Y. Lee, C. W. Lin and C. T. Lee, Aluminum-nanosphere-stacked MgNiO metal-semiconductor-metal ultraviolet photodetectors, *J. Alloys Compd*, 2019, **773**, 210-216.
13 H. Chen, P. Yu, Z. Zhang, F. Teng, L. Zheng, K. Hu and X. Fang, Ultrasensitive Self-Powered Solar-Blind Deep-Ultraviolet Photodetector Based on All-Solid-State Polyaniline/MgZnO Bilayer, *Small*, 2016, **12**, 5809-5816.
14 J. Kazmi, A. Abbas, D. James Young, J. Hussain Shah, W. Ahmad, S. Shoaib Ahmad Shah, S. Raza Ali Raza, M. Ambri Mohamed, A. O. Govorov and Z. Wang, ZnO nanowire UV photodetectors:

ARTICLE

At the intersection of flexibility, biocompatibility, and visible blindness, *Mater. Today*, 2025, **82**, 139-180.

15 S. Wang, L. Li, W. Weng, C. Ji, X. Liu, Z. Sun, W. Lin, M. Hong and J. Luo, Trilayered Lead Chloride Perovskite Ferroelectric Affording Self-Powered Visible-Blind Ultraviolet Photodetection with Large Zero-Bias Photocurrent, *J. Am. Chem. Soc*, 2020, **142**, 55-59.

16 Q. Guan, P. Xu, B. Xu, H. Ye, Z. K. Zhu, S. Wang, C. Zhang, H. Li, C. Ji, Z. Lin and J. Luo, Unprecedented Ultraviolet Circularly Polarized Light-Dependent Anomalous Photovoltaics in Chiral Hybrid Perovskites, *Adv. Sci*, 2025, **12**, 2412506.

17 Z. Xu, W. Weng, Y. Li, X. Liu, T. Yang, M. Li, X. Huang, J. Luo and Z. Sun, 3D-to-2D Dimensional Reduction for Exploiting a Multilayered Perovskite Ferroelectric toward Polarized-Light Detection in the Solar-Blind Ultraviolet Region, *Angew. Chem. Int. Ed*, 2020, **59**, 21693-21697.

18 D. Fu, W. Jia, S. Wu, J. Chang, Z. Chen and J. Luo, Bilayered Dion-Jacobson Hybrid Perovskite Bulk Single Crystals Constructed with Aromatic Diammonium for Ultraviolet-Visible-Near-Infrared Photodetection, *Chem. Mater*, 2023, **35**, 2541-2548.

19 C. Ji, D. Dey, Y. Peng, X. Liu, L. Li, J. Luo, *Angew. Chem. Int. Ed*, 2020, 59(43), 18933-18937.

20 J. J. Yoo, G. Seo, M. R. Chua, T. G. Park, Y. Lu, F. Rotermund, Y. K. Kim, C. S. Moon, N. J. Jeon, J. P. Correa-Baena, V. Bulović, S. S. Shin, M. G. Bawendi, J. Seo, *Nature*, 2021, 590(7847), 587-593.

21 G. A. Elbaz, D. B. Straus, O. E. Semonin, T. D. Hull, D. W. Paley, P. Kim, J. S. Owen, C. R. Kagan, X. Roy, *Nano Lett*, 2017, 17(3), 1727-1732.

22 M. Jaysankar, B. A. L. Raul, J. Bastos, C. Burgess, C. Weijtens, M. Creatore, T. Aernouts, Y. Kuang, R. Gehlhaar, A. Hadipour, J. Poortmans, *ACS Energy Letters*, 2019, 4(1), 259-264.

23 D. Sudarsan, R. Ganguly, A. L. Koner, S. K. Batabyal, *Adv. Mater Technologies*, 2025, 10(11), 2401573.

24 G. Maculan, A. D. Sheikh, A. L. Abdelhady, M. I. Saidaminov, M. A. Haque, B. Murali, E. Alarousu, O. F. Mohammed, T. Wu, O. M. Bakr, *Phys. Chem. Lett*, 2015, 6(19), 3781-3786.

25 J. He, S. Jiang, L. Lu, W. Li, J. Zhang, W. Wei, Z. Guo, B. Hu, Z. Wan, Y. Yun, Y. Tian, K. Huang, M. Chen, C. Li, *Nanotechnology*, 2023, 34(31), 315202.

26 L. Gao, K. Zeng, J. Guo, C. Ge, J. Du, Y. Zhao, C. Chen, H. Deng, Y. He, H. Song, G. Niu, J. Tang, *Nano Lett*, 2016, 16(12), 7446-7454.

27 J. Zhang, J. Zhao, Y. Zhou, Y. Wang, K. S. Blankenagel, X. Wang, M. Tabassum, L. Su, *Adv. Opt. Mater*, 2021, 9(17), 2100524.

28 L. Tang, W. Weng, H. Chen, L. Hua, W. Guo, Y. Liu, Y. Ma, Y. Chen, J. Luo, Z. Sun, *Adv. Funct. Mater.*, 2023, 33(22), 2214858.

29 X. Zhou, Z. Lu, L. Zhang, Q. Ke, *Nano Energ*, 2023, 117, 108908.

30 L. Liang, X. Niu, X. Zhang, Z. Wang, J. Wu, J. Luo, *Adv. Opt. Mater*, 2022, 10(24), 2201342.

31 L. Lu, W. Weng, Y. Ma, Y. Liu, S. Han, X. Liu, H. Xu, W. Lin, Z. Sun, J. Luo, *Angew. Chem. Int. Ed*, 2022, 61(26), e2205030.

32 Y. Wang, B. Su, G. Lin, H. Lou, S. Wang, C. Y. Yue, X. Lei, *CrystEngComm*, 2021, 24(12), 2258-2263.

33 C. C. Stoumpos, M. G. Kanatzidis, *Adv. Mater*, 2016, 28(28), 5778-5793.

34 V. M. Goldschmidt, *Naturwissensenschaffen*, 1926, 14 (21), 477-485.

35 S. Meloni, T. Moehl, W. Tress, M. Franckeviius, M. Saliba, Y. H. Lee, P. Gao, M. K. Nazeeruddin, S. M. Zakeeruddin, U. Rothlisberger, M. Graetzel, *Nat. Commun*, 2016, 7, 10334.

36 Q. Guan, S. You, Z. K. Zhu, R. Li, H. Ye, C. Zhang, H. Li, C. Ji, X. Liu, J. Luo, *Angew. Chem. Int. Ed*, 2024, 63(11), e202320180.

37 D. Umeyama, L. Leppert, B. A. Connor, M. A. Manumpil, J. B. Neaton, H. I. Karunadasa, *Angew. Chem. Int. Ed*, 2020, 59(43), 19087-19094.

38 J. Lv, X. Lu, X. Li, M. Xu, J. Zhong, X. Zheng, Y. Shi, X. Zhang, Q. Zhang, *Small*, 2022, 18(27), 2201715.

39 Y. Zhang, S. Li, Z. Li, H. Liu, X. Liu, J. Chen, X. Fang, *Nano Lett*, 2021, 21(1), 382-388.

40 Y. Wang, C. Ji, X. Liu, S. Han, J. Zhang, Z. Sun, A. Khan, J. Luo, *Inorg. Chem. Front*, 2018, 5(10), 2450-2455.

41 Q. Wang, H. Wang, M. Sun, R. Xue, M. Ning, S. li, P. Chen, Z. Li, *Opt Mater*, 2023, 145, 114408.

42 T. Guo, C. Tian, S. Zhao, Z. Chu, J. Ma, Y. Li, Z. Shi, G. Ran, *Phys. Chem. C*, 2021, 125(25), 13909-13916.

43 X. Li, M. Kepenekian, L. Li, H. Dong, C. C. Stoumpos, R. Seshadri, C. Katan, P. Guo, J. Even, M. G. Kanatzidis, *J.Am.Chem.Soc*, 2022, 144(9), 3902-3912.

44 A. Wang, C. Zhang, Q. Guan, H. Ye, R. Li, H. Li, Y. Geng, C. Qu, Z. Wang, C. Ji, J. Luo, *Small*, 2024, 21, 2407843.

45 L. Xu, D. Wang, H. Ye, H. Li, C. Zhang, Q. Guan, H. Zhong, Z. Han, J. Luo, *Small*, 2025, 21(9), 2410517.

46 S. Guan, Y. Li, C. Xu, N. Yin, C. Xu, C. Wang, M. Wang, Y. Xu, Q. Chen, D. Wang, L. Zuo, H. Chen, *Adv. Mater*, 2024, 36(25), 2400342.

47 X. Meng, J. Lin, X. Liu, X. He, Y. Wang, T. Noda, T. Wu, X. Yang, L. Han, *Adv. Mater*, 2019, 31(42), 1903721.

48 K. Dong, X. Yang, F. Yao, H. Cong, H. Zhou, S. Zhou, H. Cui, S. Wang, C. Tao, C. Sun, H. Fu, G. Ke, G. Fang, *Adv. Mater*, 2024, 36(24), 2313889.

49 C. Zhang, H. Xiao, Q. Guan, T. Zhu, L. Liang, R. Li, H. Ye, X. Niu, J. Luo, *Journal of Materials Chemistry C*, 2023, 11(15), 5116-5122.

50 A. Glushkova, A. Arakcheeva, P. Pattison, M. Kollár, P. Andričević, B. Náfrádi, L. Forró, E. Horváth, *CrystEngComm*, 2018, 20(25), 3543-3549.

51 Y. Tian, X. Zhang, K. Zhao, X. Miao, T. Deng, W. Fan, D. Jin, X. Jiang, S. Zhong, X. Wang, S. Wang, P. Shi, L. Tian, L. Yao, S. Gong, X. Yu, X. Gao, Z. Chen, X. Chen, Y. Lu, V. Shrote, Y. Yang, D. Yang, R. Wang, J. Xue, *Nature Photonics*, 2024, 18(9), 960-966.

52 L. Zhao, Y. Zhou, Z. Shi, Z. Ni, M. Wang, Y. Liu, J. Huang, *Nature Photonics*, 2023, 17(4), 315-323.

53 C. Ji, S. Wang, Y. Wang, H. Chen, L. Li, Z. Sun, Y. Sui, S. Wang, J. Luo, *Adv. Funct. Mater.*, 2020, 30(5), 1905529.

54 J. Sworakowski, K. Pigon, *Solid State Communications*, 1969, 30, 491-496.

55 A. Jaffe, Y. Lin, C. M. Beavers, J. Voss, W. L. Mao, H. I. Karunadasa, *ACS Central Science*, 2016, 2(4), 201-209.

56 G. Cen, Y. Liu, C. Zhao, G. Wang, Y. Fu, G. Yan, Y. Yuan, C. Su, Z. Zhao, W. Mai, *Small*, 2019, 15(36), 1902135.

57 Y. Liu, Y. Zhang, K. Zhao, Z. Yang, J. Feng, X. Zhang, K. Wang, L. Meng, H. Ye, M. Liu, S. (Frank) Liu, *Adv. Mater*, 2018, 30(29), 1707314.

58 Y. Li, T. Yang, Z. Xu, X. Liu, X. Huang, S. Han, Y. Liu, M. Li, J. Luo, Z. Sun, *Angewandte Chemie-International Edition*, 2020, 132(9), 3457-3461.

59 S. Lim, M. Ha, Y. Lee, H. Ko, *Adv. Opt. Mater*, 2018, 6(21), 1800615.

The data supporting this article have been included as part of the Supplementary
Information. For example, additional computational details and experimental details, materials, and methods, including crystal morphology, crystal structure data, PXRD patterns, the TG curve, and basic photoelectric properties.